

B.S. LUK¹, YANCHUK¹,
N. ARNOLD²,
S.M. HUANG¹,
Z.B. WANG¹,
M.H. HONG¹

Three-dimensional effects in dry laser cleaning

¹ Data Storage Institute, Agency for Science, Technology and Research, Singapore 117608
² Angewandte Physik, J. Kepler University, Altenbergerstraße 69, 4040, Linz, Austria

Received: 27 January 2003 / Accepted: 8 February 2003
Published online: 28 May 2003 • © Springer-Verlag 2003

ABSTRACT Dry laser cleaning has usually been analyzed within the framework of a one-dimensional (1D) model with homogeneous surface heating. This model gives a qualitative description of the process and is sufficient for understanding the main mechanisms. More detailed studies show that the 1D model disagrees with experiments by one to two orders of magnitude. A particle on the surface produces an inhomogeneous intensity distribution in its vicinity due to scattering and diffraction. For example, a small transparent particle can work as a lens, even in the near-field. Consequently, a non-stationary 3D distribution of the temperature and non-stationary 3D thermal deformations of the surface are produced. The 3D model developed here is qualitatively different from the 1D model (the latter does not permit the inward motion of the surface). In some region of parameter space, the 3D model predicts results close to those of experiment.

PACS 42.62.Cf; 81.65.Cf; 68.35.Np

1 Introduction

Previous theoretical examinations of dry laser cleaning have been performed for two situations: (1) thermal expansion of an absorbing particle on a transparent substrate and (2) expansion of an absorbing substrate with non-absorbing particles [1–5]. But in both cases it was assumed that the presence of the particle only weakly changes the distribution of intensity. The resulting 1D model provides a correct qualitative understanding of the main features of the dry laser cleaning problem. Nevertheless this simple model is often insufficient for explaining the experimental values of the cleaning threshold. The reason for this discrepancy is related to the scattering of radiation by contaminant particles, which strongly changes the local distribution of the absorbed laser intensity. For example, a small transparent particle can work as a near-field lens, which leads to a strong field enhancement [6, 7]. A non-stationary 3D distribution of temperature and non-stationary 3D thermal deformation of the surface are produced as a result. This requires a more detailed theoretical

analysis of the 3D effects in dry laser cleaning. In the present paper we analyze some characteristic features related to 3D effects.

2 Light focusing and near-field enhancement

As was shown in [6–12], a particle significantly changes the local intensity distribution. There are two easily understandable limiting cases. The first one refers to the geometrical optics limit, in which the size of the particle (radius a) is significantly larger than the radiation wavelength, i.e. $a \gg \lambda$. For this case the intensity on the substrate can be estimated using ray tracing according to Snell's law and energy conservation [13]. Refracted rays form a caustic (Fig. 1). If one considers a sphere with a refractive index n that is not too close to 1 or 2, then the spot size w on the substrate can be

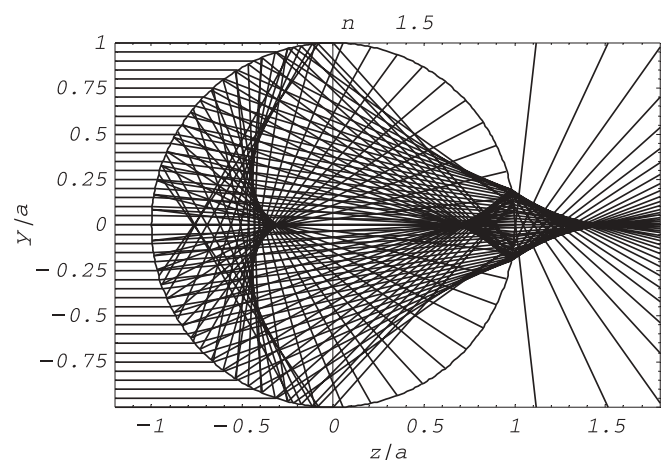


FIGURE 1 Ray tracing for a big particle $a \gg \lambda$ with refractive index $n = 1.5$. The incident angle θ_i and the refraction angle θ_t inside the sphere are related by $\theta_t = \arcsin[\sin \theta_i / n]$. Upon a second refraction the ray leaves the sphere at a point with a polar angle with respect to the z axis of $\theta_o = 2\theta_t - \theta_i$, and emerges from the sphere in the direction $\theta_{ou} = 2\theta_t - 2\theta_i < 0$. The caustic crosses the sphere at the angle θ_{om} given by the condition $\sin^2 \theta_{om} = (4 - n^2)^3 / 27n^4$. The corresponding angle of incidence θ_{im} is given by $\sin^2 \theta_{im} = (4 - n^2) / 3$. We approximate the spot size on the substrate by the caustic on the sphere: $w \approx a \sin \theta_{om}$. This yields (1). In a similar way multiple reflections can be taken into account. They produce new caustics. Within the figure the caustics inside the particle are shown for two subsequent reflections. These effects are especially important for strongly oblique rays, as they have larger reflection coefficients

✉ Fax: +65-6777/1349,
E-mail: Boris_LUKIYANCHUK@dsi.a-star.edu.sg

approximated by the caustic on the sphere:

$$w \approx a \sqrt{\frac{(4-n^2)^3}{27n^4}}. \quad (1)$$

Assuming that the intensity within the caustic cone is homogenized by the imperfections of the sphere, reflections from the substrate, etc., one can find for the intensity enhancement factor [13]:

$$\frac{I_m}{I_0} \approx \frac{a^2}{w^2} \approx \frac{27n^4}{(4-n^2)^3}. \quad (2)$$

Further modifications of this approach can be developed, taking into account secondary scattering effects related to reflection of radiation from the substrate, caustics from multiple reflection, etc.

Another useful limit follows from the dipole approximation for small spheres, i.e. $a \ll \lambda$ [14]. The corresponding polarizability δ is given by

$$\delta = 4\pi a^3 \frac{n^2 - 1}{n^2 + 2}. \quad (3)$$

Using the formulas for scattered dipole radiation and considering interference with the incident plane wave, one can find the corresponding intensity distribution (see Fig. 2). The intensity can be defined as the square of the electrical field vector, $I \propto \mathbf{E}\mathbf{E}^*$, or as the z -component of the Poynting vector, $I = S_z$, where $\mathbf{S} \propto \text{Re}[\mathbf{E}\mathbf{H}^*]$. Although the enhancement values are close to each other, one can see from Fig. 2 that these distributions are different: the square of the field has two maxima, while the Poynting vector distribution is close to a Gaussian.

At the right side of the sphere at $z = a$ (see in Fig. 1), the maximum intensity $|\mathbf{E}|^2$ enhancement in the simplest approximation (which does not produce two maxima) is given

by [13]

$$\frac{I_m}{I_0} \approx \left(1 + \frac{n^2 - 1}{n^2 + 2} q^2\right)^2. \quad (4)$$

Here $q = 2\pi a/\lambda$ is the size parameter. Comparison of (2) and (4) shows that for a refractive index $1.1 < n < 1.7$, transition to the geometrical optics limit occurs for a size parameter around $3.5 < q < 5.5$. In [13] a smooth interpolation formula (transfer from the dipole approximation to geometrical optics) was suggested. Although it qualitatively explains the role of the particle size effect, the situation is more complex because of the structure of the field within the caustic cone.

For larger spheres, it is instructive to consider Mie scattering near the sphere as a diffraction pattern of a focal caustic. In [15] it was shown that this interpretation remains fruitful even for rather small spheres. The diffraction focus f_d is shifted towards the sphere, and the intensity there has an asymptotic dependence $I_{\max} \propto ka$ for large values of the Mie parameter ka . This is typical for a (strong) spherical aberration [16] as $f \propto a$ for spheres. The focal caustic is axially symmetric and highly degenerate [17]. It contains a caustic surface of revolution with $I \propto (ka)^{1/3}$, and a caustic line along the z axis. The former is due to meridional rays, while the latter is due to sagittal rays. As a result, (if $n > \sqrt{2}$) the intensity for all $a < z < f_d$ shows the same $I(z) \propto ka$ asymptotic behavior as the focal intensity I_{\max} .

For an equivalent aberrationless lens we find $I_{\max} \propto (ka)^2$ at the focal point f and a depth of focus of about λ . According to geometrical optics, the intensity decreases as $(z-f)^{-2}$. As $f \propto a$; at the surface of the sphere, $z = a$, this yields $I(a) \propto (\lambda/a)^2 (ka)^2 \propto \text{const}(n)$. Thus, a strong spherical aberration significantly decreases the focal intensity, but creates a high intensity line between the sphere and the focus. This result is also revealed by Mie calculations. This resolves the contradiction between the Mie results [12] and

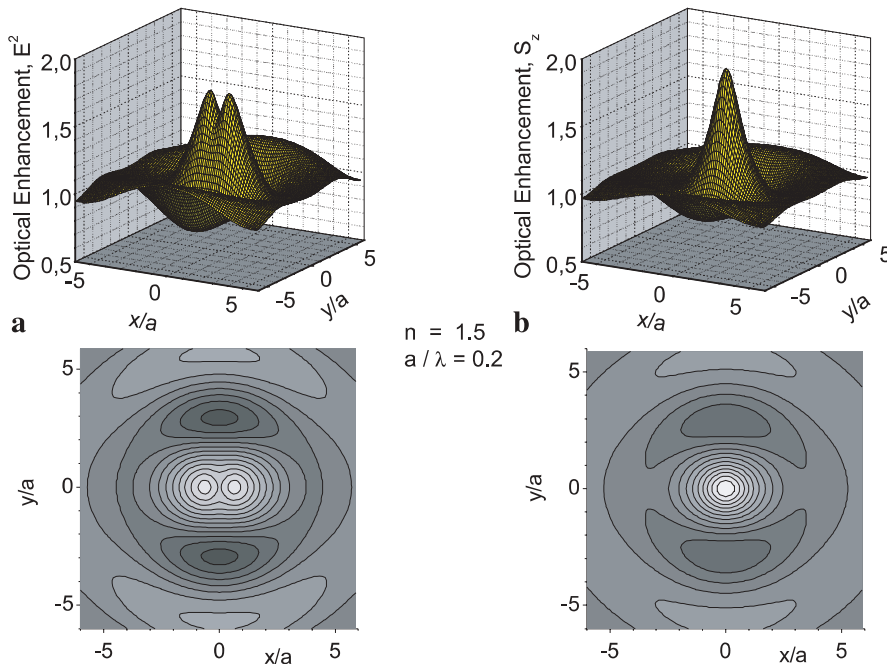


FIGURE 2 Intensity distribution in the dipole approximation for a small particle ($a/\lambda = 0.2$) with refractive index $n=1.5$. *Upper part* – 3D plot, *lower part* – contour plot. The electrical vector in the incident plane is directed along the x axis. **a** Distribution of the intensity $|\mathbf{E}|^2$ under the particle in the x - y plane; **b** Distribution of intensity (z -component of the Poynting vector) under the particle in the z - y plane. Gradations of the intensity from small (*dark*) to high (*light*) values within the contour plots are given on a logarithmic scale

estimations based on geometrical optics [13] for the intensity on the z axis behind the sphere. The prediction of geometrical optics is valid within the caustic cone, but not on the z axis. From the experimental point of view, the intensity along the z axis should be strongly decreased by imperfections or asymmetries of spheres, which destroy the degeneracy. If this is not the case, the hottest spot under the sphere has a diameter $\sim \lambda$ and intensity $\propto ka$, surrounded by a plateau of (still enhanced) intensity with parameters described by the geometrical optics results (1) and (2), and a caustic cone along its circumference.

Additional corrections to this picture are due to optical resonance effect (see, e.g. [18, 19]). Optical resonances can be understood as resonances of the waves undergoing total internal reflection. The evanescent tails of these waves leaking outside the sphere may lead to a significant variation of the near-field intensity behind the particle. These variations depend on the size parameter (see Fig. 3), while the limit of geometrical optics, i.e. (2), demonstrates only the dependence on the refractive index.

The near-field focusing is well described by the Mie theory [18]. In Fig. 4, we show the intensity distribution around a small particle, calculated from the corresponding Mie formulas. One can see the localization of energy in the region, which is smaller than the radiation wavelength (near-field focusing). The enhanced near-field intensity distribution in the x - y plane under the particle is rather complex [6–9]. Nevertheless the distribution of the z -component of the Poynting vector under the particle in the x - y plane can quite often be approximated with sufficient accuracy by a Gaussian function [12]:

$$S(x, y) = S_0 e^{-r^2/r_0^2}. \quad (5)$$

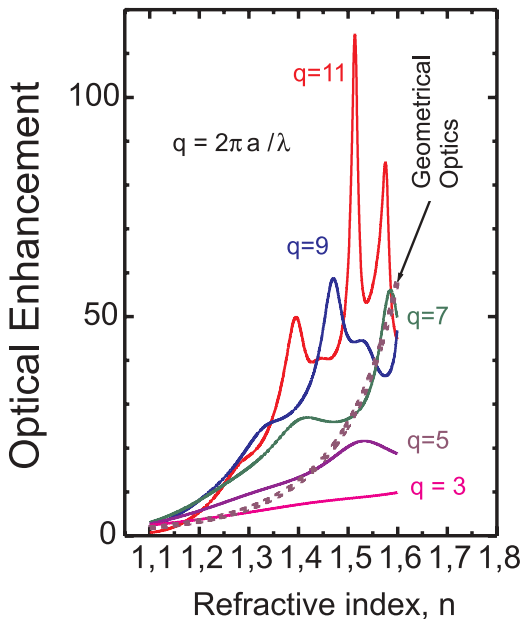


FIGURE 3 Optical enhancement under the particle versus refractive index. The *solid lines* were calculated from the Mie theory for different values of the size parameter q . The *dashed curve* is the approximation of geometrical optics calculated from (2)

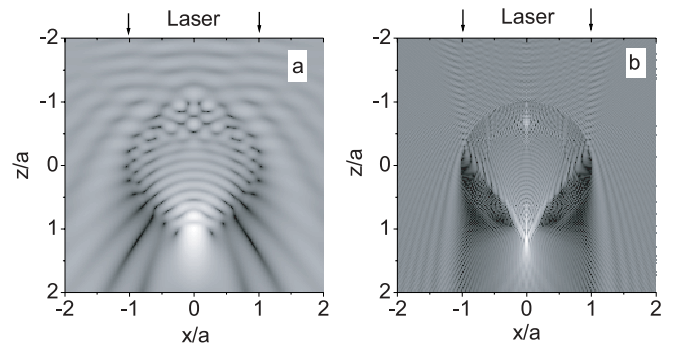


FIGURE 4 The intensity distribution $|E|^2$ (z axis along the radiation wavevector) around the particle with refractive index $n = 1.6$. The radiation wavelength is $\lambda = 248$ nm. Gradations of the intensity from small (*dark*) to high (*light*) values are on a logarithmic scale. The particle radius is $a = 0.5 \mu\text{m}$ (a) and $5 \mu\text{m}$ (b)

Here r is the radial coordinate and S_0 is the intensity enhancement factor. Distributions of the intensity (from the Mie theory) have different widths along the x and y directions (see Fig. 5a). Nevertheless we approximate the total field by a Gaussian with $r_0 = \sqrt{x_0 y_0}$. S_0 and r_0 oscillate as functions of the size parameter due to the optical resonance effect (see Figs. 5b and 6). We define averaged values (ℓ is characteristic interval for averaging) by

$$\langle S_0(a) \rangle = \frac{1}{2\ell} \int_{a-\ell}^{a+\ell} S_0(a_1) da_1, \quad \langle r_0(a) \rangle = \frac{1}{2\ell} \int_{a-\ell}^{a+\ell} r_0(a_1) da_1. \quad (6)$$

This averaging smears out the optical resonance oscillations with $\ell > \lambda/10$ (λ is the radiation wavelength). Averaged values of S_0 and r_0 (with $\ell = \lambda$) are shown in the insets of Fig. 6. It is interesting to note that in some intermediate range of small particles the averaged value of r_0 is close to constant. For example within the range of SiO_2 particle sizes from 0.1 to $10 \mu\text{m}$ ($\lambda = 248$ nm), the characteristic averaged value of the Gaussian radius was $\langle r_0 \rangle = 50 \pm 10$ nm (see Fig. 6b). Thus,

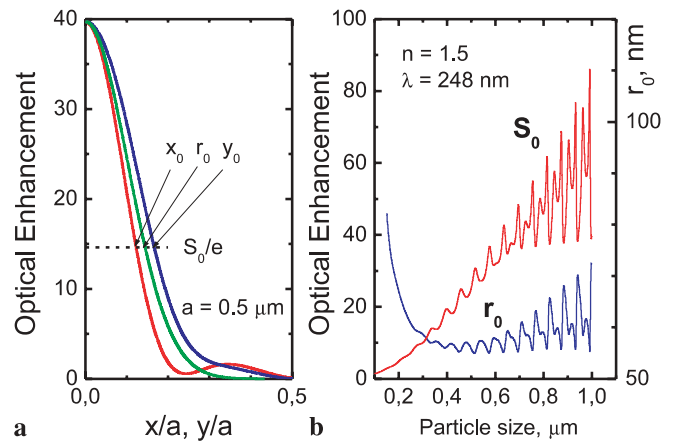


FIGURE 5 a Field enhancement factor S_0 calculated from the Mie theory and the intensity distributions along the x - and y -directions. The refractive index is $n = 1.5$ and the radiation wavelength is $\lambda = 248$ nm. b Field enhancement factor S_0 and the corresponding width $r_0 = \sqrt{x_0 y_0}$ versus particle size

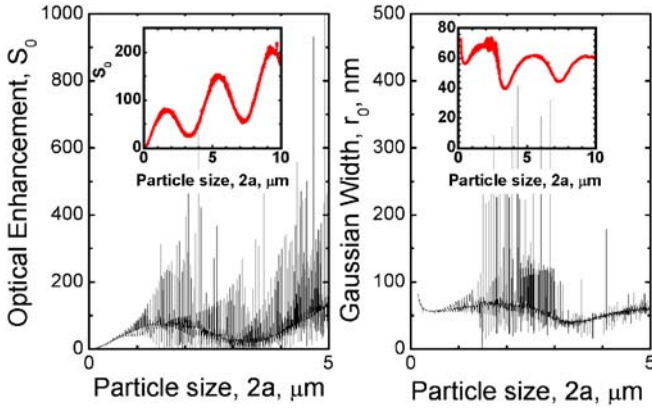


FIGURE 6 Field enhancement factor S_0 (a) and the corresponding Gaussian width $r_0 = \sqrt{\chi_0 y_0}$ (b) versus particle size for large particles. Parameters are as in Fig. 5. The insets show averaged values according to (6) with $\ell = \lambda/10$

as a first approximation one can consider $r_0 = \text{const}$. Then, for particles that are not too large (but not in the geometrical optical limit) optical enhancement can be estimated from the overall energy conservation [12, 20].

3 Temperature under the particle

The temperature rise under the particle is important for further analysis. It leads to thermal expansion of the material, i.e., to thermal deformations and stresses. Thus, we have to discuss the temperature distribution within the substrate, $T = T(x, y, z, t)$, in more detail. It can be found from the heat equation:

$$c_s \rho_s \dot{T} = \text{div} [\kappa_s \text{grad } T] + \alpha A_0 I(x, y, t) e^{-\alpha z}, \quad (7)$$

$$T|_{z=\infty} = T|_{x,y=\pm\infty} = T|_{t=0} = 0,$$

where the “dot” stands for the time derivative, and the surface intensity is in general understood to be the z -component of the Poynting vector near the substrate:

$$I(x, y, t) = S_z(x, y) I_0(t). \quad (8)$$

For a linear heat equation the solution can be expressed via a Green’s function. For a nonlinear case, for which material properties – specific heat c_s , density ρ_s , thermal conductivity κ_s , absorptivity A_0 , and absorption coefficient α – depend on temperature, (8) has to be solved numerically, which requires a large calculation time. In the case of the Gaussian profile (5), the solution of the linear heat equation can be expressed by the formula

$$T(r, z, t) = S_0 \frac{A_0 \alpha}{c_s \rho_s} \int_0^t dt_1 I_0(t-t_1) \frac{e^{-\frac{r^2}{r_0^2 + 4\chi t_1}}}{1 + 4\chi t_1 / r_0^2} F(z, t_1), \quad (9)$$

where $\chi = \kappa_s / c_s \rho_s$ is the thermal diffusivity of the substrate, and the function F is given by

$$F(z, t) = \frac{1}{2} e^{\alpha^2 \chi t} \left\{ e^{\alpha z} \text{erfc} \left[\alpha \sqrt{\chi t} + \frac{z}{2\sqrt{\chi t}} \right] + e^{-\alpha z} \text{erfc} \left[\alpha \sqrt{\chi t} - \frac{z}{2\sqrt{\chi t}} \right] \right\}. \quad (10)$$

The smooth pulse shape $I_0(t)$ typical for an excimer laser can be described by [21]

$$I_0(t) = \frac{\Phi t}{t_\ell^2} \exp \left[-\frac{t}{t_\ell} \right], \quad (11)$$

where $t_\ell = 0.409 t_{\text{FWHM}}$ (t_{FWHM} is the duration of the pulse defined at the full width at half maximum), and Φ is the (homogeneous) laser fluence incident on the sample.

In reality, the intensity under the particle has a more complex distribution than the simple Gaussian (5). Far from the particle, scattering does not influence the intensity distribution. Thus, one can consider that the enhancement effect arises due to redistribution of intensity within the “shadow” region. In our papers [8, 12, 20] we suggested approximating the total intensity distribution by a sum of three Gaussian distributions:

$$I(r, t) = I_0(t) \left[1 + S_0 e^{-r^2/r_0^2} - S_1 e^{-r^2/r_{\text{sh}}^2} \right]. \quad (12)$$

This approximation consists of 3 parts: (1) out of the particle at $r > r_{\text{sh}} \approx a + \lambda$ it tends to the homogeneous 1D intensity I_0 ; (2) in the region of enhanced radiation at $r < r_0$ it tends to the enhanced field intensity $S_0 I_0$; (3) in the “shadow” region, $r_0 < r < r_{\text{sh}}$, the intensity is rather small. This approximation neglects the oscillations within the shadow region and at the particle edge. We calculate values of S_0 and r_0 from the Mie theory, while the value $S_1 = \frac{r_0^2}{r_{\text{sh}}^2} S_0$ follows from the overall energy conservation. We call this distribution (12) the “1D + 3D model”, or simply the “3D model”.

The total temperature T can then be presented as the sum of three distributions, $T = T_{1D} + T_{3D} - T_{\text{SH}}$. All values are calculated from the 3D expression (9). For the 1D temperature T_{1D} one should put $r_0 = \infty$ and $S_0 = 1$. The effect of the shadow T_{SH} is modeled by (9) with $r_0 \rightarrow r_{\text{sh}} = a + \lambda$ and $S_0 \rightarrow S_1$. An example of a calculation of the central temperature rise with the intensity distribution (12) is shown in Fig. 7a. One can see that the 3D distribution produces a faster heating and cooling, which is important for laser cleaning.

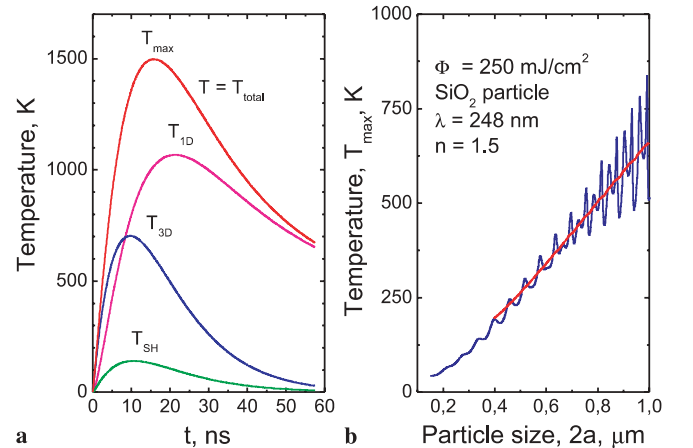


FIGURE 7 a) Temperature profile at the central point under the particle, calculated with the linear heat equation. The contribution of different terms is shown. Parameters used in the calculations: $\Phi = 1 \text{ J/cm}^2$, $S_0 = 20$, $r_0 = 50 \text{ nm}$. b) Maximal temperature under the particle, calculated with the field enhancement factor S_0 and width r_0 from Fig. 6. The averaged value is also shown

With a fixed fluence, the maximal temperature calculated from the “1D + 3D model” oscillates as a function of the particle size (see Fig. 7b). Solving the linear heat equation we have used parameters of Si at $T = 300$ K. The temperature calculated numerically from the non-linear heat equation [22] is higher, mainly because of the strong decrease in the thermal conductivity of Si with temperature. Oscillations in temperature can be more pronounced due to reflections of light from the substrate, which lead to higher intensity variations [12]. Within the 1D model, the maximal temperature does not depend on the particle size at all.

4 Dynamics of the particle and 3D effects

When the substrate expands, the position of the substrate surface, z_s , varies with time, i.e. $z_s = z_s(t)$, $z_s(0) = 0$. If the displacement of the particle center is denoted as $f(t)$, the varying deformation parameter $\delta(t)$ at time t can be expressed as

$$\delta(t) = z_s(t) + \Delta a(t) - f(t) + \delta_0. \quad (13)$$

Here the term $\Delta a(t) = \alpha_T^{(p)} a T_s(t)$ describes the effect of particle heating due to thermal contact. We assume an ideal thermal contact, for which the temperature of the particle is the same as the substrate temperature [7]. $\alpha_T^{(p)}$ is the linear thermal expansion coefficient for the particle (we use the additional superscript to distinguish the particle and substrate materials). If no external load acts on the particle, the initial deformation parameter δ_0 is expressed in the DMT theory [3] as

$$\delta_0 = \frac{1}{8} \left[\frac{9a \langle \hbar \omega \rangle^2}{2\pi^2 h^4 E^*} \right]^{1/3}, \quad \frac{1}{E^*} = \left(\frac{1 - \sigma_p^2}{E_p} + \frac{1 - \sigma_s^2}{E_s} \right), \quad (14)$$

where σ_p and σ_s , and E_p and E_s are the Poisson coefficients and Young's moduli, respectively, for the particle (p) and substrate (s), $\langle \hbar \omega \rangle$ is the Lifshitz constant, and $h \sim 0.4$ nm is the separation between the surfaces in contact.

The acceleration due to the combined elastic and adhesive force can be found from [3]:

$$\frac{4}{3} \pi a^3 \rho_p \frac{d^2 f(t)}{dt^2} = \frac{4}{3} \sqrt{a} E^* [\delta(t)^{3/2} - \delta_0^{3/2}], \quad (15)$$

where ρ_p is the density of the particle. The last (constant) term here reflects the fact that the Van der Waals component of the adhesion force is independent of deformation. The initial conditions for (15) are

$$\frac{df}{dt} \Big|_{t=0} = \frac{d\Delta a}{dt} \Big|_{t=0} = f \Big|_{t=0} = 0. \quad (16)$$

A slightly different approximation was adopted in [4,5]. There, (15) was written in a non-inertial reference frame fixed with respect to the substrate, and the macroscopic elastic-adhesion potential U was expressed as a function of the deformation $\delta(t)$. In this approach $\delta(t)$ “moves” in the adhesive potential under the action of the time dependent cleaning force

of “inertia” F_i due to thermal expansion:

$$\frac{4}{3} \pi a^3 \rho_p \frac{d^2 \delta(t)}{dt^2} = F_i - \frac{\partial U}{\partial \delta},$$

$$F_i = \frac{4}{3} \pi a^3 \rho_p \left(\frac{d^2 z_s(t)}{dt^2} + \frac{d^2 \Delta a(t)}{dt^2} \right), \quad (17)$$

where the adhesion potential $U(\delta)$ is given by

$$U(\delta) = U_0 \left[\frac{2}{5} \left(\frac{\delta}{\delta_0} \right)^{5/2} - \frac{\delta}{\delta_0} \right], \quad U_0 = \frac{4}{3} \sqrt{a} E^* \delta_0^{5/2}. \quad (18)$$

The potential $U(\delta)$ is shown in Fig. 8.

To find the epicentral surface displacement $z_s(t)$ we shall use the solution of the 3D thermal elasticity problem [4, 5, 13] which relates x - y Fourier transforms (denoted by tilde) with wavevector \mathbf{k} of the surface thermal expansion and temperature rise distribution, $\tilde{z}_s = \beta_3 \int_0^\infty e^{-kz} \tilde{T}(z) dz$, $\beta_3 = 2\alpha_T^{(s)} (1 + \sigma_s)$.

Substituting here the solution of the 3D heat equation (9) and performing direct and inverse Fourier transforms (i.e., zero-order Hankel transforms for axial symmetry, inverse transform for $r = 0$ only), one obtains

$$z_s(t) = S_0 \frac{\beta_3 A_0}{c_s \rho_s} \int_0^t \frac{I(t-t_1) dt_1}{1 + 4\chi t_1 / r_0^2} \times \int_0^\infty \alpha dz \left[1 - \sqrt{\pi} \zeta e^{\zeta^2} \operatorname{erfc}(\zeta) \right] F(z, t_1), \quad (19)$$

where r_0 is the radius of the Gaussian beam, $\zeta = \frac{z/r_0}{\sqrt{1 + 4\chi t_1 / r_0^2}}$,

and the function F is given by (10). Another approach, which yields the surface velocity, and is more convenient for the for-

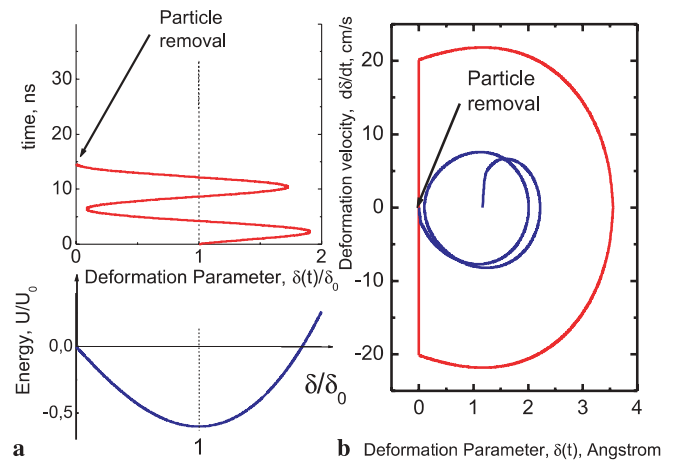


FIGURE 8 **a** Dynamics of the SiO_2 particle movement with size $2a = 1 \mu\text{m}$ on the Si substrate with the 3D+1D model. The laser fluence is 215 mJ/cm^2 and the pulse duration is 23 ns. The near-field light intensity is modeled as a Gaussian beam with enhancement factor $S_0 = 58.6$ and radius $r_0 = 63.1$ nm (Mie theory values). With fluence slightly higher than 215 mJ/cm^2 , the particle is removed at $t = 14.6$ ns during the second oscillation. The potential U is shown on the bottom part. **b** Energy criterion and phase trajectory of the system for the same parameters as in **a**

malism used in [4, 5], was adopted in [13]. There, the differential equation for $z_s(t)$ was derived. Expression (A.4) from this reference in the current notation reads

$$\dot{z}_s = \frac{\beta_3 A_0}{c_s \rho_s} \left[\frac{\alpha}{\alpha + k} \tilde{I}(0, t) - k \alpha \chi \times \int_0^t e^{\chi(\alpha^2 - k^2)t_1} \operatorname{erfc}(\alpha \sqrt{\chi t_1}) \tilde{I}(0, t - t_1) dt_1 \right]. \quad (20)$$

Substituting here the Fourier image of the Gaussian beam and performing the inversion for $r = 0$, one obtains for the epicentral surface velocity

$$\dot{z}_s(t) = S_0 \frac{\beta_3 A_0}{c_s \rho_s} \left[I(t) \int_0^\infty \frac{\alpha}{\alpha + k} \frac{r_0^2 e^{-k^2 r_0^2/4}}{2} k dk - \sqrt{\pi} \frac{\alpha \chi}{r_0} \int_0^t \frac{e^{\alpha^2 \chi t_1} \operatorname{erfc}(\alpha \sqrt{\chi t_1})}{(1 + 4\chi t_1/r_0^2)^{3/2}} I(t - t_1) dt_1 \right]. \quad (21)$$

The first integral here can be written as $\xi \left[\sqrt{\pi} + \xi e^{-\xi^2} (\operatorname{Ei}(\xi^2) - \pi \operatorname{erfi}(\xi)) \right]$ with $\xi = \alpha r_0/2$. The fact that the time derivative of (19) yields (21) is interesting on its own. In numerical calculations, we considered the smooth pulse shape, given by (11). Due to the linearity of the problem the three terms in the spatial intensity distribution produce three terms in the temperature, $T = T_{1D} + T_{3D} - T_{SH}$, and three corresponding terms for surface deformation, $z_s = z_{1D} + z_{3D} - z_{SH}$. The value of z_{3D} is calculated using (19). z_{SH} is obtained from a similar formula, with $r_0 \rightarrow r_{sh} = a + \lambda$ and $S_0 \rightarrow S_1$. The one-dimensional deformation z_{1D} is calculated by integration of (11):

$$z_{1D}(t) = \frac{\beta_3 \Phi A_0}{c_s \rho_s} \left[1 - \left(1 + \frac{t}{t_\ell} \right) \exp \left[-\frac{t}{t_\ell} \right] \right]. \quad (22)$$

The coefficient in this formula corresponds to the so-called “quasi-one-dimensional” case, in which the size of the beam is large but not infinite (see details in [5]).

Numerical integration of (15) shows (see in Fig. 8) that the particle may perform oscillations with a period of a few nanoseconds [7, 8, 12]. This period decreases approximately linearly with the particle size. These oscillations are due to the existence of a native frequency for the system of the particle on the surface. Corresponding approximate expressions are given in [4, 5, 13].

The results of integration demonstrate that the 3D model typically produces a higher deformation parameter and faster surface expansion. Different conditions for the particle removal can be written from force and energetic considerations [3, 5, 12, 13]. The force criterion considers the “static” condition for the particle removal (inertial force exceeds the Van der Waals force of attraction):

$$\frac{4}{3} \pi a^3 \rho_p \frac{d^2 f(t)}{dt^2} > F_{vdw} = \frac{\langle \hbar \omega \rangle a}{8\pi h^2}. \quad (23)$$

The energy criterion assumes that the particle is “thrown out” from a potential hole or at the expense of a critical deformation, $\delta \leq 0$, or at the expense of a loss of kinetic energy sufficient to overcome an energy barrier. The latest condition can be written in the form [23]

$$\frac{8}{15} E^* \sqrt{a \delta(t)^5} + \frac{4}{3} \pi a^3 \frac{\rho_p v^2}{2} \geq \frac{1}{2} \frac{\langle \hbar \omega \rangle a}{8\pi h^2} \delta(t) + \frac{\langle \hbar \omega \rangle a}{8\pi h}. \quad (24)$$

Here v is a relative velocity: $v = \dot{\delta}(t)$. The energy criterion can be expressed as a boundary in the $\{\delta, \dot{\delta}\}$ plane (Fig. 8b). The particle removal occurs when the phase trajectory crosses this boundary. In the range of the particle parameters discussed below, the two criteria yield very close threshold fluences (the force criterion yields a slightly smaller fluence).

Figure 9 compares the experimental and theoretical dependencies of the threshold fluence on the pulse duration and particle size. Here we use for the 3D model an intensity in the form of (12) and the three corresponding terms in (17). One can see that the 3D theory predicts thresholds an order of magnitude lower than those in the 1D theory. For NiP particles calculations show a result close to the ex-

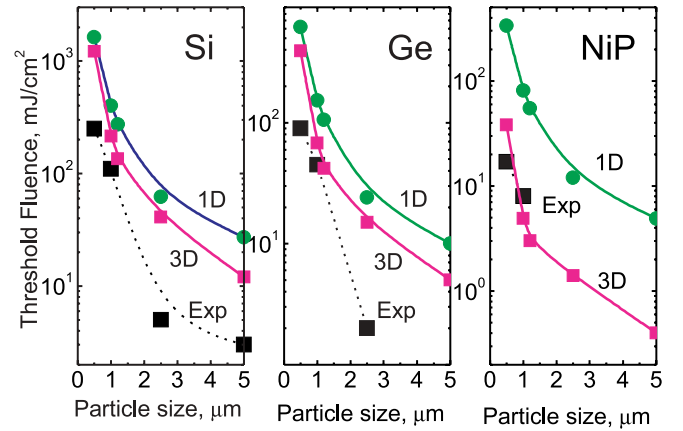


FIGURE 9 Theoretical (for 1D and 3D+1D models) and experimental results of the threshold laser fluences for SiO₂ particles on Si, Ge, and NiP substrates for a 248 nm excimer laser with a pulse duration of 23 ns

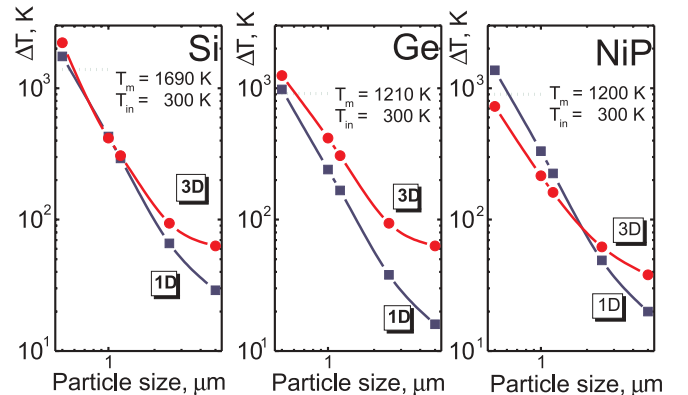


FIGURE 10 Maximal surface temperature (for 1D and 3D models) at threshold fluences, which were presented in Fig. 9

periment. For Si and Ge substrates deviations can be related to the non-linearities of the heat conduction equation. Scattering of reflected radiation also influences the optical enhancement [12]. We have to add that the number of available experimental points is insufficient to draw a definitive conclusion.

For small particles with sizes $< 0.5 \mu\text{m}$ the removal mechanism (for the Si substrate) is probably different from the thermal expansion model. It could be due to evaporation of the material under the particle [9]. Indeed, estimated temperatures of the surface at threshold fluence exceed melting or even boiling temperatures (Fig. 10). Particle removal can also be due to melting of material under the particle. This may lead to changes in adhesion properties and splashing of liquid. This mechanism is intermediate between those based on thermal elasticity and evaporation. Splashed liquid can be seen on the SEM images.

5 Conclusion

The 3D (3D+1D) model of dry laser cleaning was developed. This model takes into account the field enhancement effect, 3D thermal elasticity effects, and the true temporal pulse shape. The cleaning threshold found from this model for particles with sizes around $1 \mu\text{m}$ is significantly closer to experiment than that obtained with the conventional 1D model, which yields discrepancies of 1–2 orders of magnitude.

ACKNOWLEDGEMENTS We are very thankful to Prof. D. Bäuerle for numerous discussions. Financial support was provided by the “Austrian Fonds zur Förderung der wissenschaftlichen Forschung” project #P14700-TPH, EU TMR project Laser Cleaning #ERBFMRXCT98 0188 and in part by Russian Foundation for Basis Research (Grant Nos. 01-02-16136 and 01-02-16189).

REFERENCES

- 1 J.D. Kelley, F.E. Hovis: *Microelectron. Eng.* **20**, 159 (1993)
- 2 Y.F. Lu, W.D. Song, B.W. Ang, M.H. Hong, S.S.H. Chan, T. Low: *Appl. Phys. A* **65**, 9 (1997)
- 3 Y.F. Lu, Y.W. Zheng, W.D. Song: *J. Appl. Phys.* **87**, 1534 (2000)
- 4 N. Arnold, G. Schrems, T. Mühlberger, M. Bertsch, M. Mosbacher, P. Leiderer, D. Bäuerle: *Proc. SPIE* **4426**, 340 (2002)
- 5 N. Arnold: ‘Dry laser cleaning of particles by nanosecond pulses: Theory’. In *Laser Cleaning*, ed by B. Luk'yanchuk (World Scientific, New Jersey, London 2002) Chapt. 2, pp. 51–102
- 6 B.S. Luk'yanchuk, Y.W. Zheng, Y.F. Lu: *Proc. SPIE* **4065**, 576 (2000)
- 7 B.S. Luk'yanchuk, Y.W. Zheng, Y.F. Lu: *Proc. SPIE* **4423**, 115 (2001)
- 8 B.S. Luk'yanchuk, Y.W. Zheng, Y.F. Lu: *RIKEN Rev.* **43**, 28 (2002)
- 9 P. Leiderer, J. Boneberg, V. Döbler, M. Mosbacher, H.-J. Münzer, N. Chaoui, J. Siegel, J. Solis, C.N. Afonso, T. Fourier, G. Schrems, D. Bäuerle: *Proc. SPIE* **4065**, 249 (2000)
- 10 Y.F. Lu, L. Zhang, W.D. Song, Y.W. Zheng, B.S. Luk'yanchuk: *JETP Lett.* **72**, 658 (2000)
- 11 M. Mosbacher, H.-J. Münzer, J. Zimmermann, J. Solis, J. Boneberg, P. Leiderer: *Appl. Phys. A* **72**, 41 (2001)
- 12 B.S. Luk'yanchuk, M. Mosbacher, Y.W. Zheng, H.-J. Münzer, S.M. Huang, M. Bertsch, W.D. Song, Z.B. Wang, Y.F. Lu, O. Dubbers, J. Boneberg, P. Leiderer, M.H. Hong, T.C. Chong: In *Laser Cleaning*, ed. by B.S. Luk'yanchuk (World Scientific, New Jersey, London 2002) Chapt. 3, pp. 103–178
- 13 N. Arnold: *Appl. Surf. Sci.* **208–209**, 15 (2003)
- 14 L.D. Landau, E.M. Lifshitz, L.P. Pitaevskii: *Electrodynamics of Continuous Media* (Pergamon Press, New York 1984)
- 15 N. Arnold, R. Denk, K. Piglmayer, D. Bäuerle: to be published
- 16 Y.A. Kravtsov, Y.I. Orlov: *Geometrical Optics of Inhomogeneous Media* (Springer, Berlin 1990)
- 17 M.V. Berry, C. Upstill: In *Progress in Optics, Vol. 18*, ed. by E. Wolf (Elsevier, North-Holland 1980)
- 18 M. Born, E. Wolf: *Principles of Optics*, 7th edn. (Cambridge University Press, Cambridge 1999)
- 19 M. Kerker: ‘Selected Papers on Light Scattering’. *Proc. SPIE* **951** (Part One), (1989), see Sect. 4: ‘Optical Resonances’
- 20 B.S. Luk'yanchuk, S.M. Huang, M.H. Hong: *Proc. SPIE* **4760**, 204 (2002)
- 21 D. Bäuerle: *Laser Processing and Chemistry*, 3rd edn. (Springer-Verlag, Berlin 2000)
- 22 Y.W. Zheng, *Laser Assisted Removal of Microparticles from Solid Substrates*, PhD Thesis, National University of Singapore, 2002
- 23 Y.F. Lu, Y.W. Zheng, W.D. Song: *Appl. Phys. A* **87**, 569 (1999)